Synthesis-Controlled Cation Solubility in the Solid Sodium Ion Conductors Na_{2+x}Zr_{1-x}In_xCl₆

Tong Zhao, ^{a,b} Alexander N. Sobolev, ^a Roman Schlem, ^a Bianca Helm, ^a Marvin A. Kraft, ^c Wolfgang G. Zeier*^{a,c}

^aInstitute of Inorganic and Analytical Chemistry, University of Münster, Corrensstrasse 28/30, 48149 Münster, Germany.

^bInternational Graduate School of Battery Chemistry, Characterization, Analysis, Recycling and Application (BACCARA), University of Münster, 48149 Münster, Germany

^cInstitut für Energie- und Klimaforschung (IEK), IEK-12: Helmholtz-Institut Münster, Forschungszentrum Jülich, 48149 Münster, Germany.

*wzeier@uni-muenster.de

Abstract

Mechanochemically synthesized sodium halide solid solution with the general formula $Na_{2+x}Zr_{1-x}M_xCl_6$, as a class of potential catholytes, show promising ionic transport in comparison to its parental materials such as Na_3YCl_6 . However, the influence of subsequent heat treatment protocols on the structure and transport properties of these materials is still not fully understood. In this work, a series of $Na_{2+x}Zr_{1-x}In_xCl_6$ solid solutions is prepared by ball milling with subsequent annealing at different temperatures. The X-ray diffraction analyses show a full indium solubility in $Na_{2+x}Zr_{1-x}In_xCl_6$ when synthesized at low temperatures and crystallizing in the $P2_1/n$ phase. In contrast, at higher heat treatment temperatures exsolution is observed as the indium-rich $Na_{2+x}Zr_{1-x}In_xCl_6$ compound tends to partially transform to the trigonal $P\overline{3}1c$ phase. By assessing the ionic conductivity of the differently synthesized $Na_{2+x}Zr_{1-x}In_xCl_6$ series, we can show the synergistic effect of the $Na^+/vacancy$ ratio and crystallinity on sodium ion transport in this class of materials.

Keywords

sodium ionic conductor, cation solubility, solid electrolyte, sodium halide, ball milling, annealing temperature

Introduction

All-solid-state batteries are viewed as a promising alternative for the currently commercialized lithium-ion batteries that employ liquid electrolytes, because of their potential higher energy density and expected superior safety. 1-3 Owing to the earth-abundance of sodium, sodium solidstate batteries are promising in specific application scenarios, such as large-scale energy storage facility, where numerous low-cost and long-lasting batteries are needed.⁴ As a core component of solid-state batteries, solid electrolytes require high ionic conductivity, low electronic conductivity and electrochemical stability under work conditions, as well as chemical and mechanical compatibility with the active materials.⁵ Therefore, developing sodium solid electrolytes to meet these requirements is critical for achieving a practical application of sodium solid-state batteries. For instance, NASICON-type (e.g. NaZr₂(PO₄)₃), $^{6, 7}$ Na₃PnCh₄ (Pn = P, Sb, Ch = S, Se), $^{8-10}$ $Na_{11}Sn_2PS_{12}$ -type $^{11-13}$ and sodium closo-borate (e.g. $Na_2B_{12}H_{12})^{14,\ 15}$ have been widely explored. As an example, tungsten substitution in Na₃SbS₄ leads to an ionic conductivity of up to 41 mS·cm⁻¹ at room temperature. 16, 17 However, the inferior electrochemical stability of these sulfide solid electrolytes may lead to incompatibility with the high-voltage cathode active materials.^{4, 18, 19} In contrast, oxide-based Na⁺ conductors have wider electrochemical stability window; however, the necessary high sintering temperatures together with non-beneficial mechanical properties as well as the significant grain boundary resistances do not favor their practical application.²⁰

Recently, rare-earth-containing halides have attracted a growing interest for a potential application as solid electrolyte.²¹ The breakthrough of halide solid electrolytes stems from the work of Asano *et al.* who used high-energy ball milling and subsequent heat treatment to synthesize Li₃YCl₆ and Li₃YBr₆ with high room temperature ionic conductivities of 0.03-1.7×10⁻³ S cm⁻¹.²² To further improve the transport performance of these halide solid electrolytes, the influence of the mechanochemical synthesis protocol was subsequently investigated. For instance, ball-milling induced cation disorder, which was quantified with pair distribution function, in Li₃ErCl₆ increased the conductivity from 1.7×10⁻⁵ S·cm⁻¹ to 3.1×10⁻⁴ S·cm⁻¹.²³ Nevertheless, recent work in Li₃YCl₆ suggests that these materials are heavily influenced by stacking faults in the milled samples which can be healed at elevated temperatures.²⁴ In general, the subsequent annealing seems to exhibit a significant impact on the structure and transport properties of ball-milled lithium transition metal halides. For example, Li₃YbCl₆ heat-treated at 400 °C crystalizes in the trigonal phase while a heat-treatment at 500 °C leads to the orthorhombic phase, showing only a negligible difference in the

Li⁺ conductivity (0.19 vs. 0.15 mS cm⁻¹) and activation energy (0.47 vs. 0.53 eV).²⁵ Aliovalent substitution is a common-use strategy to improve the ionic transport properties of ionic conductors. Introducing Hf⁴⁺ in Li₃YbCl₆ increases the room temperature ionic conductivity to 1.5 mS cm⁻¹, while lowering the low activation energy to 0.26 eV and the solid state battery employing Hf-doped Li₃YbCl₆ as catholyte shows a capacity retention of 83.6% after 1000 cycles.²⁵ The encouraging results of using lithium halides as catholytes led to the increased interest and investigation of sodium halides as sodium-ion conducting solid electrolytes.²⁵⁻²⁷ So far, only a limited range of sodium transition metal halide solid solution with the general formula Na_{2+x}Zr_{1-x}M_xCl₆ (M = Y or Er) were experimentally investigated to work at room temperature. Here, Na_{2.25}Zr_{0.75}Y_{0.25}Cl₆ and Na_{2.4}Zr_{0.6}Er_{0.4}Cl₆ show ionic conductivities of 6.6×10^{-5} and 3.5×10^{-5} S·cm⁻¹ respectively, both of which crystallize in the space group $P2_1/n$.^{28, 29} Further, it has been shown that the heat treatment in Na_{2.25}Zr_{0.75}Y_{0.25}Cl₆ strongly affects the resulting phase-formation.³⁰ Nevertheless, the influence of subsequent heating protocol on the structure and transport properties of these mechanochemically synthesized sodium halide solid solutions is less explored compared to their lithium counterpart.

Motivated by the interesting properties of these Na⁺-conducting halides, the series of solid solutions of Na_{2+x}Zr_{1-x}In_xCl₆ ($0 \le x \le 1$) is investigated. By using a combination of X-ray diffraction and impedance spectroscopy, we can show that the Na_{2+x}Zr_{1-x}In_xCl₆ solid solution series crystallizes in the monoclinic $P2_1/n$ space group, while the endmembers Na₂ZrCl₆ and Na₃InCl₆ crystallize in the trigonal space groups $P\overline{3}m1$ and $P\overline{3}1c$, respectively. We further show that with increased heat treatment temperature, exsolution is favored leading to a phase transition to the $P\overline{3}1c$ phase for a high indium-containing Na_{2+x}Zr_{1-x}In_xCl₆ compound at higher temperatures, whereas at lower temperatures the $P2_1/n$ remains stable. By investigating the ionic conductivity of compounds in this Na_{2+x}Zr_{1-x}In_xCl₆ series, a direct correlation between the composition and ionic transport can be observed where an optimum Na⁺/vacancy ratio leads to facilitated Na⁺ motion. This work sheds light onto the complicated phase space in this class of materials and provides further insight into how synthesis and composition affect ionic transport in halide-based ionic conductors.

Methods

Synthesis. All syntheses work was performed under an Argon atmosphere or vacuum. For the

mechanochemical synthesis, stoichiometric amounts of NaCl (Merck, 99.5%, pre-dried at 200 °C for 48 h under vacuum), InCl₃ (Merck, 99.99%), and ZrCl₄ (Merck, 99.99%) were placed into ball mill cups. The mass ratio between precursors and milling media (ZrO₂, 5 mm diameter) was 1:30. The planetary ball-milling (Fritsch Pulverisette 7) was carried out at 100 rpm for 10 minutes and 300 rpm for 10 minutes to mix the precursors uniformly. Afterwards, the ball-milling was carried out for 99 cycles in reverse mode, with one cycle including milling at 500 rpm for 15 minutes and a 5-minute-long rest for the purpose of cooling. Then, for the subsequent crystallization, the ball-milled powders were pelletized by a custom-made manual screw press and transferred into a quartz ampoule which was pre-dried at 800 °C under a dynamic vacuum for 2 hours. The ampoules were sealed under vacuum and then heated in a preheated furnace at target temperature. After annealing, the pellets were air-quenched to ensure precise heating time and subsequently hand-ground into powders for further characterization.

X-ray diffraction. All samples were sealed in glass capillaries for X-ray diffraction measurements because of their air and moisture sensitivity. X-ray diffraction for Rietveld analysis was performed with a STOE STADI P diffractometer (Mo K α 1 radiation, λ = 0.7093 Å; curved Ge(111) monochromator, Mythen detector) in Debye–Scherrer scan mode at room temperature. Data collection was carried out for every sample in 0.015° steps.

Rietveld analysis. X-ray diffraction data were refined by the Rietveld method using the TOPAS Academic software package. $^{31, 32}$ Rietveld refinements consisted of (1) background of Chebychev polynomial function, (2) scaling factor, (3) lattice parameters, (4) peak shape parameters from the modified Thompson-Cox-Hastings pseudo-Voigt function, (5) site fractional coordinates and occupancy factors, and the (6) isotropic displacement parameters. Furthermore, the isotropic thermal displacement parameters were constrained to be equal for the same atomic species. At last, all variable parameters were opened simultaneously to achieve the best possible fit. The quality of the refinements was evaluated by the indicators $R_{\rm wp}$ and goodness-of-fit (GoF). 33 All applied constraints and resulting structural information can be found tabulated in the Supporting Information.

Electrochemical impedance spectroscopy. Ionic conductivities and activation energies were extracted from temperature dependent electrochemical impedance spectroscopy. Approximately 150 mg of each sample were preliminarily pelletized by a manual screw press and then isostatically pressed under 330 MPa for 40 min. Subsequently, the pellets were contacted with thin gold electrodes by sputter deposition and then enclosed in pouch cells. The impedance measurements

were carried out by using an SP-300 impedance analyzer (Biologic) applying an amplitude of 10 mV and frequencies in the range of 7 MHz to 100 mHz. Spectra were collected at temperatures between -40 °C to 60 °C and analyzed by RelaxIS 3 (rhd instruments). To obtain reliable fitting results, the ultrahigh or ultralow frequency range was discarded based on the data quality assessed with Kramers-Kronig test (less than 2% residuals).

Bond Valence Sum Analyses. The bond valance site energies (BVSEs) were calculated by the softBV software tool.^{34, 35} The calculations were performed with the automatically estimated screening factor and a resolution of 0.1 Å.

Results and discussions

Structural analyses. Solid solutions of $Na_{2+x}Zr_{1-x}In_xCl_6$ were synthesized similarly to the reported mechanochemically assisted synthesis procedure of Na₃ErCl₆.²⁸ First, the Na_{2+x}Zr_{1-x}In_xCl₆ solid solution precursors are synthesized from NaCl, InCl₃ and ZrCl₄ using ball milling. Afterwards, the compounds are annealed for 1 h at 330 °C to crystallize. The collected powder X-ray diffraction patterns are shown in *Figure 1a*. Comparing the diffraction pattern reveals that Na₂ZrCl₆ (x = 0) crystallizes in a different crystal system than the substituted compounds. Furthermore, the diffractograms of the substitution degrees x(In) = 0.1 - 0.4 show no additional reflections being phase pure, while for x(In) = 0.5 additional reflections, marked by asterisks (*), are observed. Thus, a solubility limit of indium in the substitution series is found. To better understand the influence of the annealing temperature on the solubility of In in the target composition $Na_{2+x}Zr_{1-x}In_xCl_6$, the ball milled compounds are annealed at 200 °C as well and the collected X-ray diffraction patterns are shown in *Figure 1b*. For the compositions annealed at 200 °C, their X-ray diffraction patterns are line with main phase of those annealed at 330°C, different from both unsubstituted compounds, and no obvious additional reflections can be found in the collected diffractograms in the whole range of compositions from x = 0.1 to x = 0.9. The direct comparison of the diffraction patterns of Na_{2.5}Zr_{0.5}In_{0.5}Cl₆ annealed at different temperatures in *Figure 1c* shows that the 330 °C annealed sample has several distinct reflections at \sim 1.01, 1.05 and 1.17 Å⁻¹ which cannot be observed when annealed at 200 °C indicating the absence of the additional phase. Even though the occurring slightly lower crystallinity, resulting from the mild heating treatment, broadens the reflections in the Na_{2+x}Zr_{1-x}In_xCl₆ series annealed at 200 °C, the diffraction pattern of Na_{2.5}Zr_{0.5}In_{0.5}Cl₆ annealed at 200 °C obviously has no reflections at ~1.17 Å⁻¹ demonstrating that it does not have the side phases that are visible in the 330 °C annealed samples. To further evaluate the structural change

along the Na_{2+x}Zr_{1-x}In_xCl₆ series annealed at different temperatures, Rietveld refinements were performed (*Figure S1-2*). The Rietveld refinements shows that $Na_{2+x}Zr_{1-x}In_xCl_6$ solid solutions can crystallize in a defective cryolite structure-type of the monoclinic space group $P2_1/n$ ($P2_1/n$ phase), which is a commonly adopted phase for cation-mixed sodium halide ionic conductors, such as the Na_{2+x}Zr_{1-x}Er_xCl₆ and Na_{2+x}Zr_{1-x}Y_xCl₆ series. ^{28, 29} Interestingly, the additional phase observed in 330 °C annealed Na_{2.5}Zr_{0.5}In_{0.5}Cl₆ may be indexed as the trigonal phase (space group $P\overline{3}1c$), similar to the structure of the end member Na₃InCl₆. A disordered P31c structure with an additional sodium Wyckoff 2c site of Na₃InCl₆ formed under ~177 °C was reported previously.³⁶ However the refinement result of Na₃InCl₆ annealed at 200 °C using a disordered structure as starting model shows the sodium occupancy at Wyckoff 2c site is only $\sim 8\%$ and the statistics suggest no obvious difference with that using ordered starting model, which means the subtle structural difference determination is very likely beyond the limit of resolution of lab X-ray diffractometer. Here the disordered structure approach was discarded and a more commonly-adopted ordered Na₃InCl₆ structure was used as starting model to refine the side phase of Na_{2.5}Zr_{0.5}In_{0.5}Cl₆ annealed at 330 °C. As the refined side phase content is only $\sim 10.9(4)$ wt.%, its full composition and structure cannot be accurately determined and therefore it is unclear whether the side phase results from decomposition of the phases or an exsolution of the Na₃InCl₆ analogue. To better understand the underlying reason for this solubility affected by the annealing temperature, a phase with a much higher In content, the nominal Na_{2.9}Zr_{0.1}In_{0.9}Cl₆ was annealed at 300 °C for 2h to obtain a greater amount of side phase (*Figure S3a*). The refinement result shows that the Na₃InCl₆-type $P\overline{3}1c$ phase content of nominal Na_{2.9}Zr_{0.1}In_{0.9}Cl₆ annealed at 300 °C is ~36.5(5) wt.%. At this percentage, a refinement of the side-phase is a bit more reliable and the composition of the side phase can be identified. The Zr occupancy of $P\overline{3}1c$ phase of nominal Na_{2.9}Zr_{0.1}In_{0.9}Cl₆ annealed at 300 °C is ~13% and its refined unit cell volume is ~510 Å⁻³ while that of Na₃InCl₆ is ~513 A⁻³ suggesting a cationmixed P31c phase exsolution at higher annealing temperatures. On the contrary, Na_{2.9}Zr_{0.1}In_{0.9}Cl₆ annealed at 200 °C for 2h is determined as a pure P2₁/n phase (Figure S3a and 4). The powder Xray diffraction patterns of $Na_{2+x}Zr_{1-x}In_xCl_6$ from x = 0.6 to 0.9 annealed at 330 °C are shown in **Figure S3b** and the reflections of the $P\overline{3}1c$ phase marked by the light grey shade are more distinct in comparison to that of 330 °C annealed Na_{2.5}Zr_{0.5}In_{0.5}Cl₆. Hence, the Na_{2+x}Zr_{1-x}In_xCl₆ substitution series shows a temperature variable solubility limit, where higher indium-containing $Na_{2+x}Zr_{1-x}In_xCl_6$ samples tend to crystallize the $P\bar{3}1c$ phase at higher temperatures as illustrated in Figure S3c.

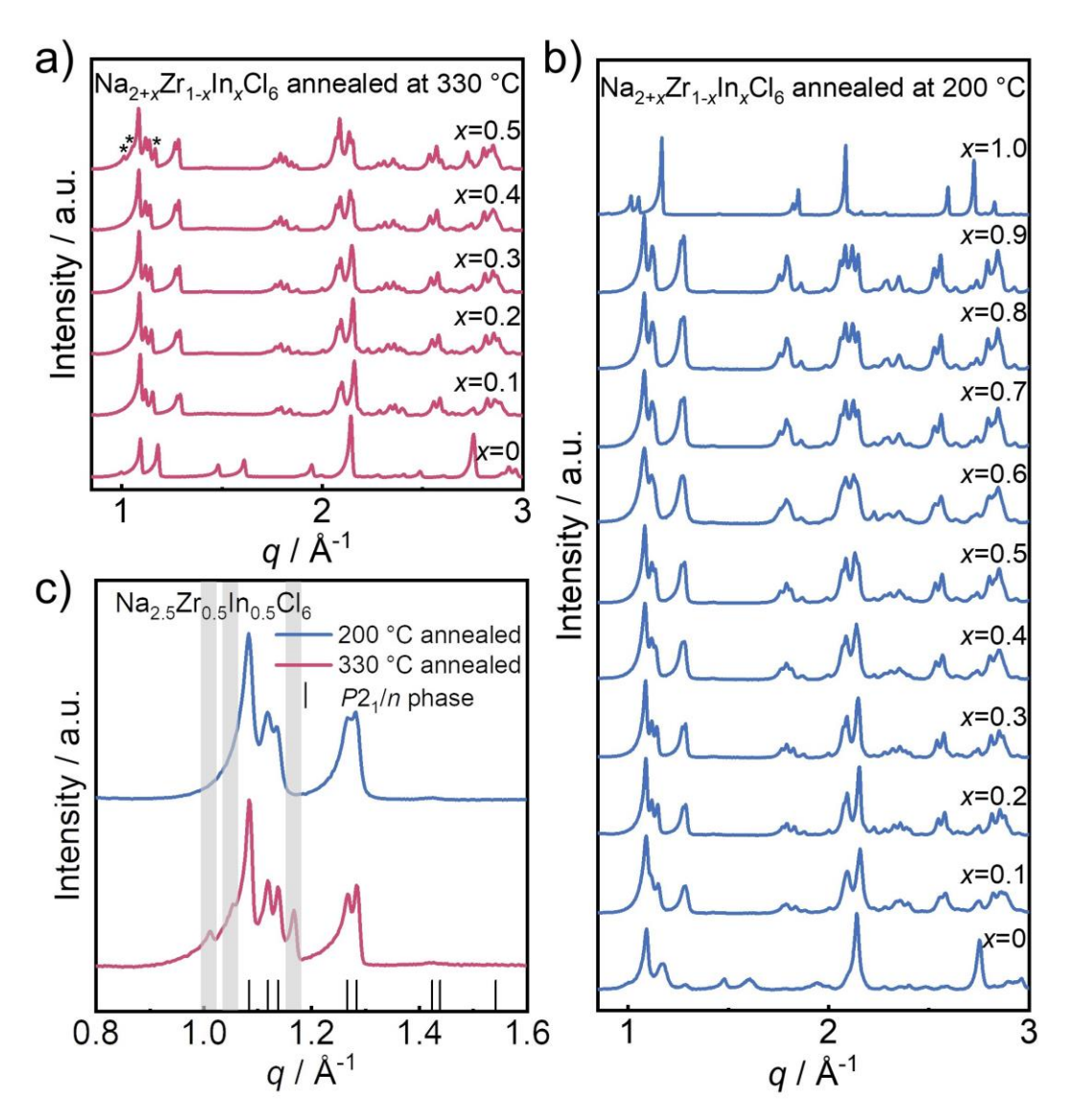


Figure 1. X-ray diffraction patterns under Mo Ka1 radiation of $Na_{2+x}Zr_{1-x}In_xCl_6$ annealed at **a)** 330 °C and **b)** 200 °C. **c)** X-ray diffraction patterns comparison of $Na_{2.5}Zr_{0.5}In_{0.5}Cl_6$ annealed at 200 °C and 330 °C.

Structure of the Na_{2+x}Zr_{1-x}In_xCl₆ solid solutions. Aliovalent substitutions are a commonly used strategy to improve transport performance. Most of the Na⁺ - conducting halide solid solutions reported as so far inherit the structure type of one of its end members. For instance Na_{2+x}Zr_{1-x}M_xCl₆ (M = Y, and Er) adopts the $P2_1/n$ phase, in line with the room temperature structures of Na₃YCl₆ and Na₃ErCl₆.^{28, 29} The ionic radii of six-fold coordinated Y³⁺ and Er³⁺ are 90 and 89 pm respectively, which are comparable.³⁷ However, the In³⁺ radius (80 pm) is significantly smaller than that of the Y³⁺ and Er³⁺. Therefore, it is intriguing that the Na_{2+x}Zr_{1-x}In_xCl₆ series still crystallizes in the monoclinic $P2_1/n$ phase, which differs significantly from both of its parental materials that

crystallize in the trigonal system, i.e. Na₂ZrCl₆ adopting $P\overline{3}m1$ phase and Na₃InCl₆ adopting $P\overline{3}1c$ phase as reported, and the refinement results are shown in *Figure S5*.^{27, 36} *Figure 2a* displays the structure of Na_{2+x}Zr_{1-x}In_xCl₆ represented by Na_{2.3}Zr_{0.7}In_{0.3}Cl₆ which consists of two In³⁺/Zr⁴⁺ ions (Wyckoff 2*a*), the stoichiometry-dependent Na⁺ ions (Wyckoff 4*e* and 2*b*), and twelve Cl⁻ ions (Wyckoff 4*e*) per unit cell (formula units per unit cell Z = 2). Zr⁴⁺ and In³⁺ ions are coordinated octahedrally by chloride anions at the corner and center of the unit cell (*Figure 2b*). NaCl₆⁵⁻ octahedra are located at the edges along c-axis and center of *ab*-planes of the unit cell, with Na⁺ at the Wyckoff 2*b* position and Cl⁻ at three separate Wyckoff 4*e* positions. While Na⁺ ions at the Wyckoff 4*e* positions are coordinated prismatically by the chloride ions (*Figure 2c*). The side phase of Na_{2.5}Zr_{0.5}In_{0.5}Cl₆ in $P\overline{3}1c$ phase, in line with the ordered Na₃InCl₆, as shown in *Figure 2d-f*. Its unit cell consists of two In³⁺/Zr⁴⁺ ions (Wyckoff 2*d*), the stoichiometry-dependent Na⁺ ions (Wyckoff 4*f* and 2*a*), and twelve Cl⁻ ions (Wyckoff 12*i*) with formula units per unit cell Z = 2. Unlike the $P2_1/n$ phase, all cations of Na_{2+x}Zr_{1-x}In_xCl₆ in the space group of $P\overline{3}1c$ are six-fold coordinated octahedrally by chloride anions.

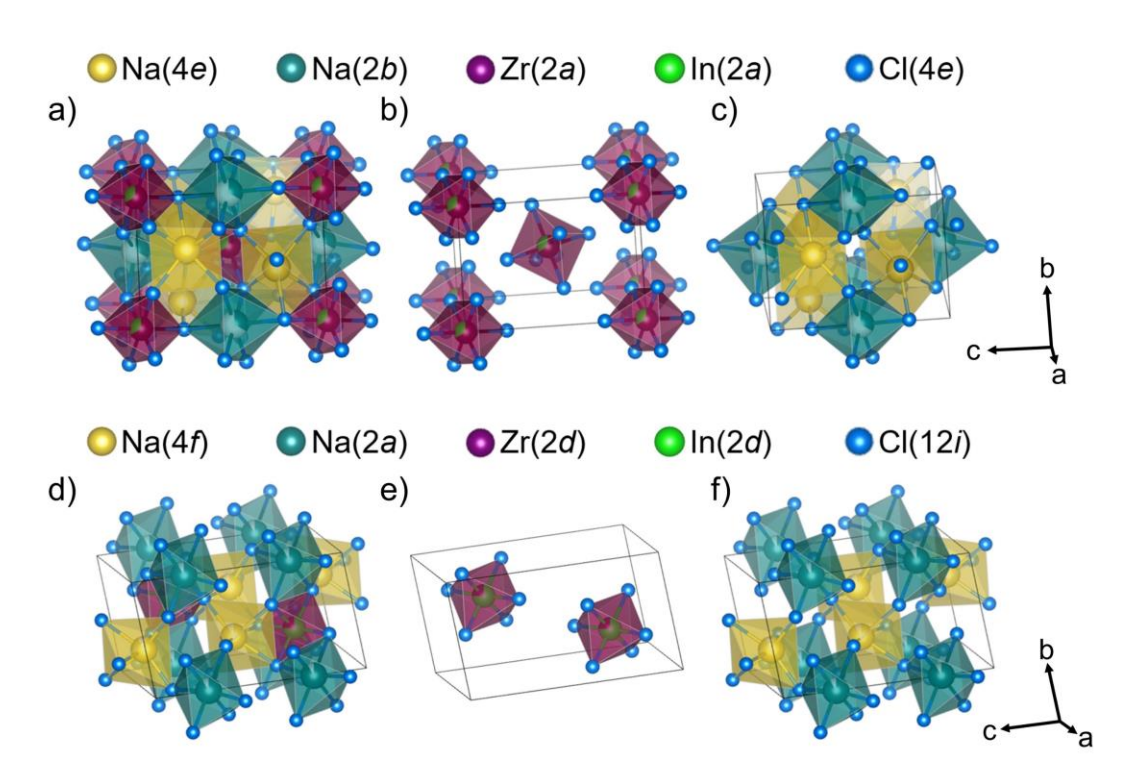


Figure 2. Top: Crystal structure of $Na_{2+x}Zr_{1-x}In_xCl_6$ in space group $P2_1/n$ represented by $Na_{2.3}Zr_{0.7}In_{0.3}Cl_6$. **a)** The full structure. **b)** The building units of $Zr_{1-x}In_xCl_6^{(2+x)-}$ octahedra, and **c)** the building units of $NaCl_6^{5-}$ octahedra and prism. **Bottom:** Crystal structure of $Na_{2+x}Zr_{1-x}In_xCl_6$ side phase in space group $P\overline{3}1c$ phase represented by nominal $Na_{2.5}Zr_{0.5}In_{0.5}Cl_6$. **d)** The full

structure. **e)** The building units of $Zr_{1-x}In_xCl_6^{(2+x)-}$ octahedra, and **f)** the building units of $NaCl_6^{5-}$ octahedra.

The evolution of the lattice parameters of the solid solutions is shown in *Figure 3. Figure 3a and b* display the refined In³⁺ fraction as a function of the nominal content of the Na_{2+x}Zr_{1-x}In_xCl₆ series annealed at 200 °C and 330 °C, respectively. An approximate linear behavior is obtained for the pure phase region of the Na_{2+x}Zr_{1-x}In_xCl₆ series annealed at either 330 °C or 200 °C, corroborating the existence of a solid solution. Because the In³⁺ radius (80 pm) is larger than that of Zr⁴⁺ (72 pm),³⁷ the lattice parameters a, b and c of Na_{2+x}Zr_{1-x}In_xCl₆ annealed at 200 °C exhibit a sharp growth upon increased In contents for the low substitution degrees (0.1 \leq \leq 0.6). This is in line with those of Na_{2+x}Zr_{1-x}In_xCl₆ (0.1 \leq \leq 0.4) annealed at 330 °C, before reaching the solubility limit. Then a flattening trend of the lattice parameters can be found with further increasing In content ($x \geq$ 0.7), meanwhile the angle β between the α and α axes show a decreasing slope against substitution degree α (*Figure 3e-f*). Similar influences of changing angles on the structure were found in Na₃ErCl₆ and Li₃InCl₆ with Zr substitution.^{28, 38}

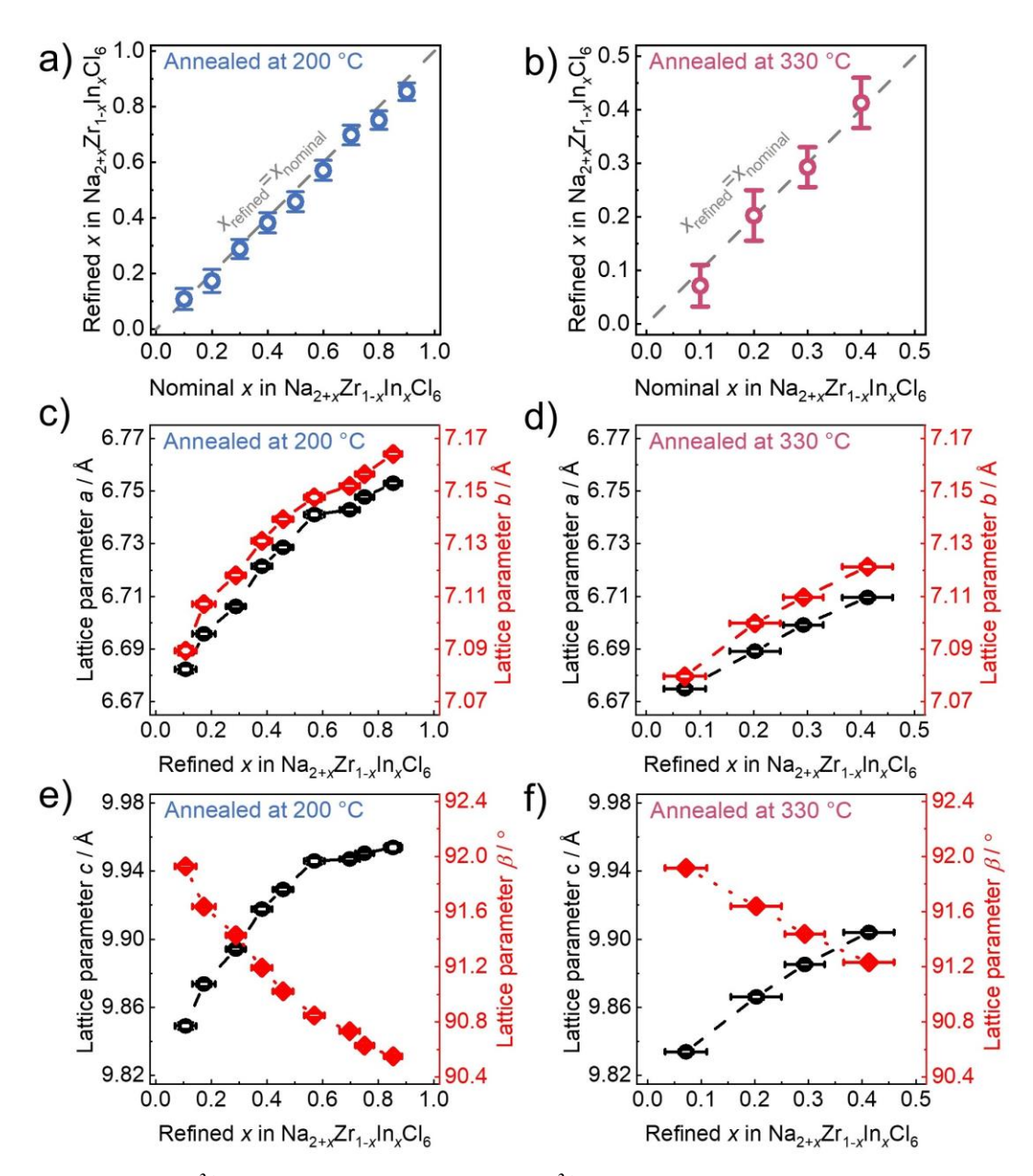


Figure 3. Refined In^{3+} content against nominal In^{3+} content of $Na_{2+x}Zr_{1-x}In_xCl_6$ annealed at a) 200 °C and b) 330 °C. Lattice parameters a and b of $Na_{2+x}Zr_{1-x}In_xCl_6$ annealed at c) 200 °C and d) 330 °C against refined In^{3+} content. Lattice parameters c and β of $Na_{2+x}Zr_{1-x}In_xCl_6$ annealed at e) 200 °C and f) 330 °C against refined In^{3+} content.

Figure 4 displays further structural evolution details of $Na_{2+x}Zr_{1-x}In_xCl_6$. The unit cell volume of $Na_{2+x}Zr_{1-x}In_xCl_6$ annealed at 200 °C is in line with that of the unit cell parameters, showing a significant growth from x = 0.1 to 0.6 and then a slowing increase between x = 0.6 and 0.9. *Figure 4b* shows the distribution of sodium ions. The Na^+ occupancy at the Wyckoff 4e site levels out at

slightly below 100% while the Na⁺ occupancy at the Wyckoff 2b position exhibits a positive correlation with indium substitution. Due to the larger radius and lower valence of In³⁺ leading to weaker electrostatic interaction with Cl^- , a quasi-linear increase of the $Zr_{1-x}In_xCl_6$ (2+x)- octahedral volume can be observed. With increasing In³⁺ content, the NaCl₆⁵⁻ octahedra (Na⁺ at Wyckoff 2b site) increases in volume until the substitution degree of x = 0.6, as shown in *Figure 4d*. Exceeding a refined In³⁺ fraction of 60%, there is a slight decrease of Na(2b)Cl₆⁵⁻ octahedral volume. As for the non-linear behavior of NaCl₆⁵⁻ polyhedral volume, it seems possible that this stems from the trade-off between unit cell length and Na⁺ occupancy at Wyckoff 2b site: (1) within $x \leq 0.6$, the sharp rise of unit cell length due to In³⁺ incorporation results in the increase of distance between octahedra Na⁺ and Zr/In ions at unit cell corner. As the octahedra Na⁺ locates at a crystallographic special position (Wyckoff 2b site), the polyhedral cannot shift, so the connecting Na-Cl bond needs to be extended, which leads to the stretching of NaCl₆⁵⁻ octahedra (as shown in *Figure S6a*), which dominates the octahedral volume change and overcomes the increased effective interaction between Wyckoff 2b Na⁺ and Cl⁻ resulting from the increasing Na⁺ occupancy at Wyckoff 2b site. (2) When x is greater than 0.6, the growth of unit cell expansion slows down while $Na^+ 2b$ occupancy still ascends steadily. Hence the increased effective Na(2b)-Cl interaction affects the Na(2b)Cl₆⁵⁻ volumes more significantly and leads to the slight reduction. The refined volume of NaCl₆⁵⁻ prism with Na⁺ located at the Wyckoff 4e site shows similar trend while its overall volume change is not as dramatic as that of NaCl₆⁵⁻ octahedra because of the almost full Wyckoff 4e site occupancy for all samples in this series. However, the In content significantly impacts the geometric features of NaCl₆⁵⁻ prism. As shown in *Figure S6b-c*, the Zr(In)1-Zr(In)2-Cl1 angle increases upon increased substitution degree while the Zr(In)1- Zr(In)2-Cl2 angle decreases, indicating counterclockwise rotation of the $Zr_{1-x}In_xCl_6^{(2+x)-}$ octahedra along the b axis, which also results in the lattice parameter β rising. In contrast, the Cl-Cl distances lengthens with the increase of In substitution, verifying the previously found influence of Zr_{1-x}In_xCl₆ (2+x)⁻ octahedral rotation on the prism distortion.²⁸ The triangular areas of the prism always play the role of bottleneck for ion movement. Both two triangular areas of Na(4e)Cl₆⁵⁻ prism reaches the largest at intermediate substitution degree (x \sim 0.6), in line with prism volume change (*Figure 4d*). Due to the low solubility of Na_{2+x}Zr_{1-x}In_xCl₆ annealed at 330 °C, the structural evolution details can only be observed within $x \le 0.4$, which shows a similar case as the 200 °C annealed series in the same region, as shown in *Figure S7a-c*.

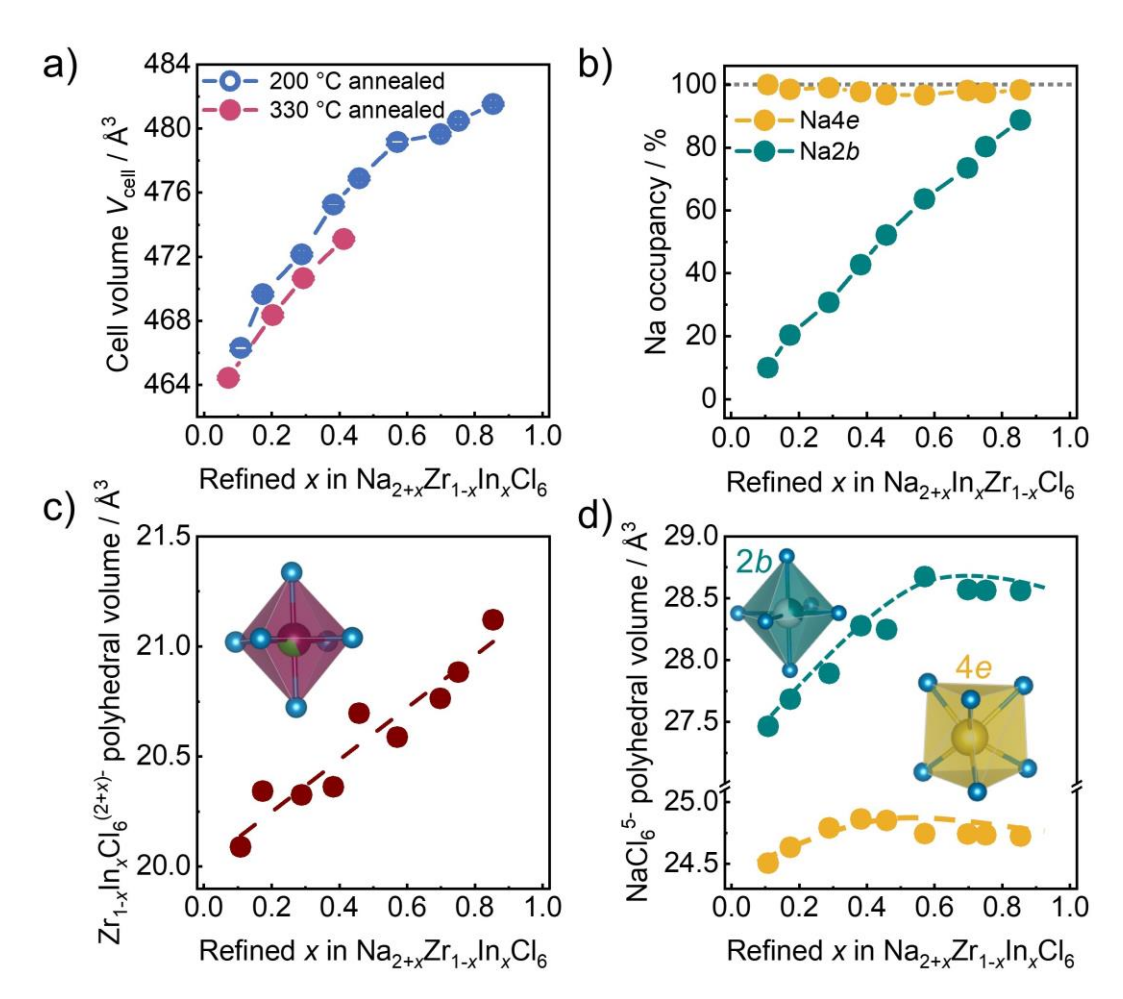


Figure 4. a) Refined cell volumes of $Na_{2+x}Zr_{1-x}In_xCl_6$ annealed at 200 °C and 330 °C. **b)** Na^+ occupancies at Wyckoff 2b and 4e sites of $Na_{2+x}Zr_{1-x}In_xCl_6$ annealed at 200 °C. **c)** The $Zr_{1-x}In_xCl_6$ (2+x)- octahedral volumes of $Na_{2+x}Zr_{1-x}In_xCl_6$ annealed at 200 °C. **d)** The $NaCl_6$ ⁵⁻ octahedra and prism volumes of $Na_{2+x}Zr_{1-x}In_xCl_6$ annealed at 200 °C.

Ionic transport properties. The Na⁺ ion transport of the Na_{2+x}Zr_{1-x}In_xCl₆ solid solution series annealed at different temperatures is evaluated using temperature-dependent electrochemical impedance spectroscopy. The collected room temperature (25 °C) impedance spectra are displayed in *Figure S8* in Nyquist representation. All impedance spectra of Na_{2+x}Zr_{1-x}In_xCl₆ annealed at 200 °C can be fit with one equivalent circuit model (the inset of *Figure S8a*) consisting of a parallel resistor-constant phase element (CPE) combination, in series with another CPE representing the blocking electrodes. The resolved impedance spectra exhibit α -values of ~0.9 representing the ideality (exponent) of the CPE and capacitances around ~1×10⁻¹⁰ F. Nevertheless, the contributions of grain bulk and grain boundary cannot be deconvoluted and the fitted capacitances do not allow the exclusion of grain boundary contributions, ³⁹ thus representing the total ionic conductivity. The

impedance spectra of Na_{2+x}Zr_{1-x}In_xCl₆ annealed at 330 °C show an additional process compared to those of 200 °C annealed samples, hence an equivalent circuit model (the inset of *Figure S8e*) consisting of two parallel resistor-constant phase element (CPE) combinations in series with another CPE is used to fit these spectra of 330 °C annealed samples. The capacitances resolved from the additional semicircle are around 1 to 6×10^{-7} F, indicating that the additional process more likely originates from the interface between electrolyte and electrode rather than grain boundaries, as previously reported.⁴⁰ For a fair comparison, the total ionic conductivity of Na_{2+x}Zr_{1-x}In_xCl₆ annealed at 330 °C was hence calculated using the fitted resistance from the high frequency process that represents a combined bulk and grain boundary contribution.

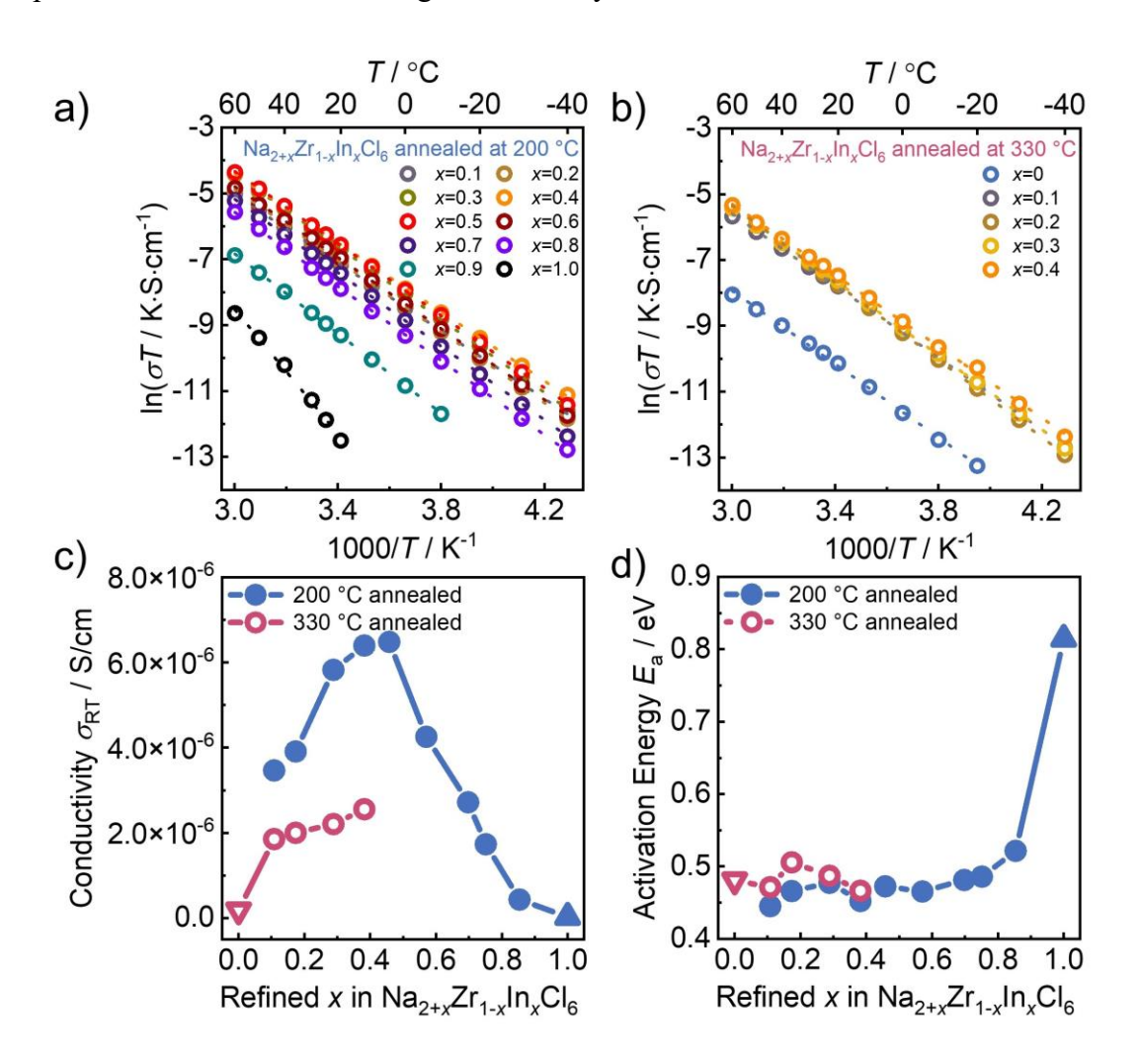


Figure 5. Arrhenius plots from the temperature dependent impedance of $Na_{2+x}Zr_{1-x}In_xCl_6$ annealed at **a)** 200 °C and **b)** 330 °C. The spectra of some samples at low temperature are too resistive to be resolved and are therefore excluded from the Arrhenius plot. **c)** Ionic conductivities and **d)** activation energies of $Na_{2+x}Zr_{1-x}In_xCl_6$ annealed 200 °C and 330 °C.

The Na⁺ conductivities of Na_{2+x}Zr_{1-x}In_xCl₆ solid solutions annealed at different temperatures show linear Arrhenius behavior in the measured temperature ranges (see *Figure 5a, b*). The obtained room-temperature conductivities and the activation energies (E_a) were extracted from the linear Arrhenius fitting, shown in *Figure 5c, d* as a function of the refined indium substitution degree. The 330 °C annealed Na_{2+x}Zr_{1-x}In_xCl₆ exhibits an increased room temperature ionic conductivity upon incorporation of indium from x = 0.1 to 0.4, meanwhile the 200 °C annealed series shows a more complex case. The room temperature ionic conductivity of Na_{2+x}Zr_{1-x}In_xCl₆ annealed at 200 °C experiences an upward trend with In content at first, reaching the peak of ~6.5×10⁻⁶ S·cm⁻¹ at x = 0.5, and then sharply decreases with further increases of the indium content. The room temperature ionic conductivity of the most conductive compound Na_{2.5}Zr_{0.5}In_{0.5}Cl₆ is three orders of magnitude larger than that of the end member Na₃InCl₆ (~2.3×10⁻⁸ S·cm⁻¹). Clearly the substitution has a significant impact on transport properties. However, the activation barrier shows different behavior. The activation energy drops from ~0.81 eV for Na₃InCl₆ to 0.52 eV for Na_{2.9}Zr_{0.1}In_{0.9}Cl₆ and then it fluctuates at around 0.45 eV for the cation-mixed Na_{2+x}Zr_{1-x}In_xCl₆ series as well as ending member Na₂ZrCl₆.

A bond valence sum approach was used to identify the possible low energy diffusion pathways in these solid ionic conductors. As shown in *Figure S9*, the bond valence sum calculations show three Na⁺ diffusion pathways: (I) a Na⁺ jump from the octahedrally coordinated Wyckoff 2b site to the Wyckoff 4e site in an edge-sharing prism. (II) an indirect transition between corner-sharing octahedra and prism involving two interstitial sites (i1, i2). (III) an octahedra-octahedra transition involving the third interstitial site i3. While the interstitial site remains unoccupied in the resolution limit of X-ray diffraction, the two Na⁺ site occupancies will be important for the ionic transport. As shown above, the Wyckoff 4e site is almost fully occupied, hence the unoccupied Wyckoff 2b sites play a major role in the vacancy-process for Na⁺ diffusion. Figure 6a shows the ionic conductivity of Na_{2+x}Zr_{1-x}In_xCl₆ series annealed at 200 °C against the Wyckoff 2b occupancy (Occ_{Na2b}), which exhibits a typical Na⁺-vacancy modulating behavior, in line with the analogues Na_{2+x}Zr_{1-x}Y_xCl₆ and Na_{2+x}Zr_{1-x}Er_xCl₆ series. ^{28, 29} When Occ_{Na2b} is less than 60%, Na⁺ carriers are insufficient in number density and the ionic conductivity shows an increasing trend with the increase of Occ_{Na2b} . Therefore, the solid solution with Wyckoff 2b site occupancy of ~50% reaches the highest conductivity. Afterwards, the ionic conductivity declines when Occ_{Na2b} further increases $(Occ_{Na2b} \ge 60\%)$. Clearly, Na⁺/vacancy ratio dominates transport performance in this materials

class with similar crystallinity. Hence, the ionic conductivity as a function of Occ_{Na2b} can fit with the model based on $Occ_{Na2b} \cdot (1-Occ_{Na2b})$ and the medium-substituted sample with greatest $Occ_{Na2b} \cdot (1-Occ_{Na2b})$ value reaches highest ionic conductivity because of the tradeoff between Na⁺ and vacancy concentration.^{29, 41} To better understand the geometric features of $Zr_{1-x}In_xCl_6^{(2+x)-}$ octahedra on ionic conductivity, its distortion is also investigated. The distortion index (D) is widely used to estimate the distortion degree of polyhedrons in crystal structures which is based on the bond lengths between the central ion and coordinating ions.⁴² The distortion index of $Zr_{1-x}In_xCl_6^{(2+x)-}$ of $Na_{2+x}Zr_{1-x}In_xCl_6$ annealed at 200°C shows a sharp growth and then levels out at ~0.006 against substitution degree. However, there is no obvious correlation between distortion of $Zr_{1-x}In_xCl_6^{(2+x)-}$ and ionic conductivity (*Figure S10*).

Nevertheless, while the synthesis temperature of 200 °C helps to reach a full solubility and with it the optimum behavior in transport as a function of the occupancies on the Wyckoff 2*b* site, the conductivities for the samples annealed at 330 °C show a similar trend in structure, Na⁺/vacancy ratios and activation barriers, but much lower ionic conductivities. At this stage we assume this is due to different crystallinities from the heat treatment protocol. Especially in these halide-based materials, the synthesis approach,²³ crystallinity,⁴³ microstrain,⁴⁴ and occurring stacking faults²⁴ play a significant role in modulating transport properties of the solid electrolyte. Therefore, the Na⁺/vacancy ratio and crystallinity synergistically affect the transport performance of the Na_{2+x}Zr_{1-x}In_xCl₆ solid solution series.

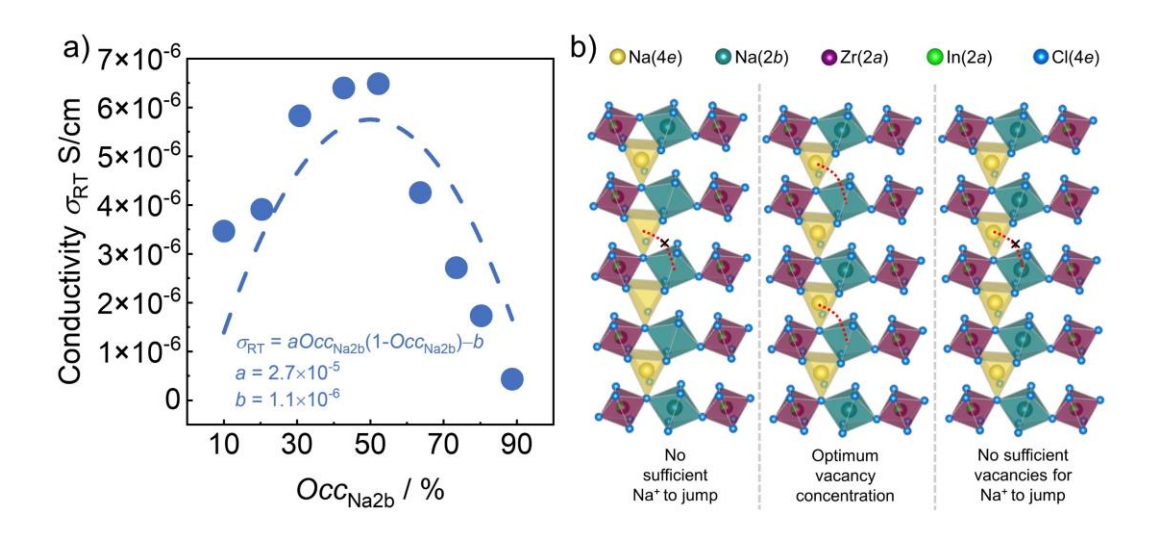


Figure 6. a) Ionic conductivities of $Na_{2+x}Zr_{1-x}In_xCl_6$ annealed 200 °C as a function of Na^+

occupancy at Wyckoff 2b site (Occ_{Na2b}). **b)** Schematic of two-dimension atomistic projection illustrating the influence of vacancy concentration on Na^+ movement.

Conclusion

In this work, we investigated the influence of the post heat treatment protocol on the solubility of indium in the ball-milled sodium metal halide solid solution series of $Na_{2+x}Zr_{1-x}In_xCl_6$. All 200 °C annealed solid solutions of $Na_{2+x}Zr_{1-x}In_xCl_6$ series can be stabilized in a pure cryolite-analogue structure (space group $P2_1/n$) while $Na_{2.5}Zr_{0.5}In_{0.5}Cl_6$ annealed at 330 °C exhibits a side phase that is found to be a polymorph in the $P\overline{3}1c$ space group. By careful heat treatment comparisons, we can show that high indium-containing $Na_{2+x}Zr_{1-x}In_xCl_6$ solid solution tends to transform to $P\overline{3}1c$ phase at higher temperatures suggesting the synthesis-dependent indium solubility of the $P2_1/n$ polymorph. By monitoring the ion transport employing impedance spectroscopy, the ionic conductivity shows a carrier-vacancy mediated mechanism and the low temperature annealed samples exhibits higher ionic conductivities likely due to lower crystallinity.

This work demonstrates that solubility of different metal ions in sodium halide solid solutions can be influenced by the heat treatment protocol subsequent to mechanochemical synthesis. Moreover, Na⁺/vacancy ratio and crystallinity are vital for the transport performance in this class of materials. These conclusions shed light on the design principle and synthesis strategy of sodium transition metal halide solid solutions as highly conductive electrolytes, aiding the development of solid-state batteries.

Acknowledgments

This work is funded by the Ministry of Culture and Science of the State North Rhine Westphalia in course of the International Graduate School of Battery Chemistry, Characterization, Analysis, Recycling and Application (BACCARA).

Supporting Information

The Supporting Information includes Rietveld refinement results, X-ray diffraction data of Na_{2.9}Zr_{0.9}In_{0.1}Cl₆ annealed at 200 °C and 300 °C, structural evolution of Na_{2+x}Zr_{1-x}In_xCl₆ annealed

at 200 °C and 330 °C, X-ray diffraction patterns of nominal $Na_{2+x}Zr_{1-x}In_xCl_6$ (x=0.6 - 1) annealed at 330 °C, scheme of the overall phases depending on the synthesis condition, the room-temperature impedance data, calculated Na^+ diffusion pathways by bond valence sum analyses, distortion index of the $Zr_{1-x}In_xCl_6$ ($^{(2+x)-}$ octahedral and its influence on ionic conductivity.

References

- 1. Schnell, J.; Günther, T.; Knoche, T.; Vieider, C.; Köhler, L.; Just, A.; Keller, M.; Passerini, S.; Reinhart, G., All-solid-state lithium-ion and lithium metal batteries paving the way to large-scale production. *J. Power Sources* **2018**, *382*, 160-175.
- 2. Janek, J.; Zeier, W. G., A solid future for battery development. *Nature Energy* **2016**, *1* (9), 16141.
- 3. Janek, J.; Zeier, W. G., Challenges in speeding up solid-state battery development. *Nature Energy* **2023**, *8* (3), 230-240.
- 4. Wang, Y.; Song, S.; Xu, C.; Hu, N.; Molenda, J.; Lu, L., Development of solid-state electrolytes for sodium-ion battery—A short review. *Nano Materials Science* **2019**, *1* (2), 91-100.
- 5. Zheng, F.; Kotobuki, M.; Song, S.; Lai, M. O.; Lu, L., Review on solid electrolytes for all-solid-state lithium-ion batteries. *J. Power Sources* **2018**, *389*, 198-213.
- 6. Guin, M.; Tietz, F., Survey of the transport properties of sodium superionic conductor materials for use in sodium batteries. *J. Power Sources* **2015**, *273*, 1056-1064.
- 7. Winand, J.-M.; Rulmont, A.; Tarte, P., Nouvelles solutions solides LI(MIV)2-x(NIV)x(PO4)3 (L = Li,Na M,N = Ge,Sn,Ti,Zr,Hf) synthèse et étude par diffraction x et conductivité ionique. *J. Solid State Chem.* **1991,** *93* (2), 341-349.
- 8. Zhu, Z.; Chu, I.-H.; Deng, Z.; Ong, S. P., Role of Na+ Interstitials and Dopants in Enhancing the Na+ Conductivity of the Cubic Na3PS4 Superionic Conductor. *Chem. Mater.* **2015**, 27 (24), 8318-8325.
- 9. Krauskopf, T.; Muy, S.; Culver, S. P.; Ohno, S.; Delaire, O.; Shao-Horn, Y.; Zeier, W. G., Comparing the Descriptors for Investigating the Influence of Lattice Dynamics on Ionic Transport Using the Superionic Conductor Na3PS4–xSex. *J. Am. Chem. Soc.* **2018**, *140* (43), 14464-14473.
- 10. Krauskopf, T.; Pompe, C.; Kraft, M. A.; Zeier, W. G., Influence of Lattice Dynamics on Na+ Transport in the Solid Electrolyte Na3PS4–xSex. *Chem. Mater.* **2017**, *29* (20), 8859-8869.
- 11. Kraft, M. A.; Gronych, L. M.; Famprikis, T.; Ohno, S.; Zeier, W. G., Structure and Sodium Ion Transport in Na11+xSn2+x(Sb1-yPy)1-xS12. *Chem. Mater.* **2020**, *32* (15), 6566-6576.
- 12. Zhang, Z.; Ramos, E.; Lalère, F.; Assoud, A.; Kaup, K.; Hartman, P.; Nazar, L. F., Na11Sn2PS12: a new solid state sodium superionic conductor. *Energy & Environmental Science* **2018**, *11* (1), 87-93.
- 13. Duchardt, M.; Ruschewitz, U.; Adams, S.; Dehnen, S.; Roling, B., Vacancy-Controlled Na+ Superion Conduction in Na11Sn2PS12. *Angew. Chem. Int. Ed.* **2018**, *57* (5), 1351-1355.
- 14. Matsuo, M.; Kuromoto, S.; Sato, T.; Oguchi, H.; Takamura, H.; Orimo, S.-i., Sodium ionic conduction in complex hydrides with [BH4]—and [NH2]—anions. **2012**, *100* (20), 203904.
- 15. Moury, R.; Lodziana, Z.; Remhof, A.; Duchene, L.; Roedern, E.; Gigante, A.; Hagemann, H., Pressure-induced phase transitions in Na2B12H12, structural investigation on a candidate for

- solid-state electrolyte. *AcCrB* **2019**, 75 (3), 406-413.
- 16. Fuchs, T.; Culver, S. P.; Till, P.; Zeier, W. G., Defect-Mediated Conductivity Enhancements in Na3–xPn1–xWxS4 (Pn = P, Sb) Using Aliovalent Substitutions. *ACS Energy Letters* **2020**, *5* (1), 146-151.
- 17. Hayashi, A.; Masuzawa, N.; Yubuchi, S.; Tsuji, F.; Hotehama, C.; Sakuda, A.; Tatsumisago, M., A sodium-ion sulfide solid electrolyte with unprecedented conductivity at room temperature. *Nature Communications* **2019**, *10* (1), 5266.
- 18. Qie, Y.; Wang, S.; Fu, S.; Xie, H.; Sun, Q.; Jena, P., Yttrium—Sodium Halides as Promising Solid-State Electrolytes with High Ionic Conductivity and Stability for Na-Ion Batteries. *The journal of physical chemistry letters* **2020**, *11* (9), 3376-3383.
- 19. Oh, J. A. S.; He, L.; Chua, B.; Zeng, K.; Lu, L., Inorganic sodium solid-state electrolyte and interface with sodium metal for room-temperature metal solid-state batteries. *Energy Storage Materials* **2021**, *34*, 28-44.
- 20. Anantharamulu, N.; Koteswara Rao, K.; Rambabu, G.; Vijaya Kumar, B.; Radha, V.; Vithal, M., A wide-ranging review on Nasicon type materials. *JMatS* **2011**, *46* (9), 2821-2837.
- 21. Li, X.; Liang, J.; Yang, X.; Adair, K. R.; Wang, C.; Zhao, F.; Sun, X., Progress and perspectives on halide lithium conductors for all-solid-state lithium batteries. *Energy & Environmental Science* **2020**, *13* (5), 1429-1461.
- 22. Asano, T.; Sakai, A.; Ouchi, S.; Sakaida, M.; Miyazaki, A.; Hasegawa, S., Solid Halide Electrolytes with High Lithium-Ion Conductivity for Application in 4 V Class Bulk-Type All-Solid-State Batteries. **2018**, *30* (44), 1803075.
- 23. Schlem, R.; Muy, S.; Prinz, N.; Banik, A.; Shao-Horn, Y.; Zobel, M.; Zeier, W. G., Mechanochemical Synthesis: A Tool to Tune Cation Site Disorder and Ionic Transport Properties of Li3MCl6 (M = Y, Er) Superionic Conductors. *Advanced Energy Materials* **2020**, *10* (6), 1903719.
- 24. Sebti, E.; Evans, H. A.; Chen, H.; Richardson, P. M.; White, K. M.; Giovine, R.; Koirala, K. P.; Xu, Y.; Gonzalez-Correa, E.; Wang, C.; Brown, C. M.; Cheetham, A. K.; Canepa, P.; Clement, R. J., Stacking Faults Assist Lithium-Ion Conduction in a Halide-Based Superionic Conductor. *J Am Chem Soc* **2022**, *144* (13), 5795-5811.
- 25. Park, J.; Han, D.; Kwak, H.; Han, Y.; Choi, Y. J.; Nam, K.-W.; Jung, Y. S., Heat treatment protocol for modulating ionic conductivity via structural evolution of Li3-xYb1-xMxCl6 (M = Hf4+, Zr4+) new halide superionic conductors for all-solid-state batteries. *Chem. Eng. J.* **2021**, *425*, 130630.
- 26. Li, X.; Liang, J.; Luo, J.; Norouzi Banis, M.; Wang, C.; Li, W.; Deng, S.; Yu, C.; Zhao, F.; Hu, Y.; Sham, T.-K.; Zhang, L.; Zhao, S.; Lu, S.; Huang, H.; Li, R.; Adair, K. R.; Sun, X., Air-stable Li3InCl6 electrolyte with high voltage compatibility for all-solid-state batteries. *Energy & Environmental Science* **2019**, *12* (9), 2665-2671.
- 27. Kwak, H.; Lyoo, J.; Park, J.; Han, Y.; Asakura, R.; Remhof, A.; Battaglia, C.; Kim, H.; Hong, S.-T.; Jung, Y. S., Na2ZrCl6 enabling highly stable 3 V all-solid-state Na-ion batteries. *Energy Storage Materials* **2021**, *37*, 47-54.
- 28. Schlem, R.; Banik, A.; Eckardt, M.; Zobel, M.; Zeier, W. G., Na3–xEr1–xZrxCl6—A Halide-Based Fast Sodium-Ion Conductor with Vacancy-Driven Ionic Transport. *ACS Applied Energy Materials* **2020**, *3* (10), 10164-10173.
- 29. Wu, E. A.; Banerjee, S.; Tang, H.; Richardson, P. M.; Doux, J.-M.; Qi, J.; Zhu, Z.; Grenier, A.; Li, Y.; Zhao, E.; Deysher, G.; Sebti, E.; Nguyen, H.; Stephens, R.; Verbist, G.; Chapman, K. W.; Clément, R. J.; Banerjee, A.; Meng, Y. S.; Ong, S. P., A stable cathode-solid electrolyte composite for high-voltage, long-cycle-life solid-state sodium-ion batteries. *Nature Communications* **2021**, *12* (1), 1256.
- 30. Sebti, E.; Qi, J.; Richardson, P. M.; Ridley, P.; Wu, E. A.; Banerjee, S.; Giovine, R.;

- Cronk, A.; Ham, S.-Y.; Meng, Y. S.; Ong, S. P.; Clément, R. J., Synthetic control of structure and conduction properties in Na–Y–Zr–Cl solid electrolytes. *Journal of Materials Chemistry A* **2022**, *10* (40), 21565-21578.
- 31. Rietveld, H. M., The Rietveld method. *Phys. Scr.* **2014**, *89* (9), 098002.
- 32. Coelho, A. A., TOPAS and TOPAS-Academic: an optimization program integrating computer algebra and crystallographic objects written in C++. *J. Appl. Crystallogr.* **2018**, *51* (1), 210-218.
- 33. Young, R. A., The Rietveld Method. Oxford University Press: New York 1993.
- 34. Chen, H.; Adams, S., Bond softness sensitive bond-valence parameters for crystal structure plausibility tests. *IUCrJ* **2017**, *4* (5), 614-625.
- 35. Chen, H.; Wong, L. L.; Adams, S., SoftBV a software tool for screening the materials genome of inorganic fast ion conductors. *AcCrB* **2019**, *75* (1), 18-33.
- 36. Yamada, K.; Kumano, K.; Okuda, T., Conduction path of the sodium ion in Na3InCl6 studied by X-ray diffraction and 23Na and 115In NMR. *Solid State Ionics* **2005**, *176* (7), 823-829.
- 37. Shannon, R., Revised effective ionic radii and systematic studies of interatomic distances in halides and chalcogenides. *AcCrA* **1976**, *32* (5), 751-767.
- 38. Helm, B.; Schlem, R.; Wankmiller, B.; Banik, A.; Gautam, A.; Ruhl, J.; Li, C.; Hansen, M. R.; Zeier, W. G., Exploring Aliovalent Substitutions in the Lithium Halide Superionic Conductor Li3 xIn1 xZrxCl6 ($0 \le x \le 0.5$). Chem. Mater. **2021**, 33 (12), 4773-4782.
- 39. Irvine, J. T. S.; Sinclair, D. C.; West, A. R., Electroceramics: Characterization by Impedance Spectroscopy. **1990**, *2* (3), 132-138.
- 40. Schlem, R.; Bernges, T.; Li, C.; Kraft, M. A.; Minafra, N.; Zeier, W. G., Lattice Dynamical Approach for Finding the Lithium Superionic Conductor Li3ErI6. *ACS Applied Energy Materials* **2020**, *3* (4), 3684-3691.
- 41. Kwak, H.; Han, D.; Lyoo, J.; Park, J.; Jung, S. H.; Han, Y.; Kwon, G.; Kim, H.; Hong, S.-T.; Nam, K.-W.; Jung, Y. S., New Cost-Effective Halide Solid Electrolytes for All-Solid-State Batteries: Mechanochemically Prepared Fe3+-Substituted Li2ZrCl6. **2021**, *11* (12), 2003190.
- 42. Baur, W., The geometry of polyhedral distortions. Predictive relationships for the phosphate group. *AcCrB* **1974**, *30* (5), 1195-1215.
- 43. Rajeswari, K.; Suresh, M. B.; Chakravarty, D.; Das, D.; Johnson, R., Effect of nano-grain size on the ionic conductivity of spark plasma sintered 8YSZ electrolyte. *Int. J. Hydrogen Energy* **2012**, *37* (1), 511-517.
- 44. Wang, C.; Liang, J.; Luo, J.; Liu, J.; Li, X.; Zhao, F.; Li, R.; Huang, H.; Zhao, S.; Zhang, L.; Wang, J.; Sun, X., A universal wet-chemistry synthesis of solid-state halide electrolytes for all-solid-state lithium-metal batteries. **2021**, *7* (37), eabh1896.

For table of contents only

